View metadata, citation and similar papers at core.ac.uk
brought to you by CORE
provided by AIR Universita degli studi di Milano

MNRAS **474,** 3391–3396 (2018)
Advance Access publication 2017 November 21
doi:10.1093/mnras/stx2950

Discovery and first models of the quadruply lensed quasar SDSS J1433+6007

Adriano Agnello,[1★] Claudio Grillo,[2,3] Tucker Jones,[4,5†] Tommaso Treu,[6‡] Mario Bonamigo[3] and Sherry H. Suyu[7,8,9]

[1]*European Southern Observatory, Karl-Schwarzschild-Strasse 2, D-85748 Garching bei München, Germany*
[2]*Dark Cosmology Centre, Niels Bohr Institute, University of Copenhagen, Juliane Maries Vej 30, DK-2100 Copenhagen, Denmark*
[3]*Dipartimento di Fisica, Università degli Studi di Milano, via Celoria 16, I-20133 Milano, Italy*
[4]*Department of Physics and Astronomy, PAB, 430 Portola Plaza, Box 951547, Los Angeles, CA 90095-1547, USA*
[5]*Department of Physics, University of California Davis, 1 Shields Avenue, Davis, CA 95616, USA*
[6]*Max-Planck-Institut für Astrophysik, Karl-Schwarzschild-Str. 1, D-85741 Garching, Germany*
[7]*Institute of Astronomy, University of Hawaii, 2680 Woodlawn Drive, Honolulu, HI 96822, USA*
[8]*Institute of Astronomy and Astrophysics, Academia Sinica, PO Box 23-141, Taipei 10617, Taiwan*
[9]*Physik-Department, Technische Universität München, James-Franck-Straße 1, D-85748 Garching, Germany*

Accepted 2017 November 13. Received 2017 November 10; in original form 2017 February 13

ABSTRACT

We report the discovery of the quadruply lensed quasar SDSS J1433+6007 (RA = 14:33:22.8, Dec. = +60:07:13.44), mined in the SDSS DR12 photometric catalogues using a novel outlier-selection technique, without prior spectroscopic or ultraviolet excess information. Discovery data obtained at the Nordic Optical Telescope (La Palma) show nearly identical quasar spectra at $z_s = 2.737 \pm 0.003$ and four quasar images in a fold configuration, one of which sits on a blue arc, with maximum separation 3.6 arcsec. The deflector redshift is $z_l = 0.407 \pm 0.002$, from Keck-ESI spectra. We describe the selection procedure, discovery and follow-up, image positions and *BVRi* magnitudes, and first results and forecasts from lens model fit to the relative image positions.

Key words: gravitational lensing: strong – methods: statistical – techniques: image processing – catalogues.

1 INTRODUCTION

Strong gravitational lensing by galaxies enables the study of distant sources and luminous and dark matter in galaxies over a range of redshifts (see e.g. Courbin, Saha & Schechter 2002, for a review). When the source is a quasar, its multiple images give a wealth of information on: the source central engine and the stellar content of the lens, via microlensing by individual stars (Wambsganss 2001; Kochanek 2004; Braibant et al. 2016; Schechter et al. 2016); substructure in the lens, via astrometric and flux-ratio 'anomalies' (Mao & Schneider 1998; Dalal & Kochanek 2002; Nierenberg et al. 2014; Xu et al. 2015; Agnello et al. 2017); quasars and their hosts at $z_s \approx 2$ (More et al. 2009; Rusu et al. 2014; Agnello et al. 2016); and from the time-delays between the light curves of different images, cosmological distances and tests of the Lambda cold dark matter concordance cosmology (Refsdal 1964; Kochanek 2003; Paraficz & Hjorth 2009; Suyu et al. 2014).

However, quasar lenses are rare, as they require the precise alignment of a distant source with (at least) a galaxy.[1] Oguri & Marshall (2010, hereafter OM10) estimate that ≈0.2 lensed quasars per square degree, brighter than $i = 21$, should be present in wide-field surveys, with a majority of doubly imaged quasars and ≈20 per cent quadruples. Quasars are rare objects themselves and are less frequent beyond redshifts $z_s \approx 1.8$ (OM10, Ménard et al. 2010), whereas quasar lenses should have source redshifts at $z \approx 2.5 \pm 0.3$, from OM10 models.

Since the first discovery of a lensed quasar (QSO 0957+561, Walsh, Carswell & Weymann 1979) in the radio, about 10^2 multiply imaged quasars have been discovered so far, with various methods in several optical and radio surveys. Some searches concentrated on bright quasars at redshift ≥1, such as the *HST* Snapshot Survey (Maoz et al. 1992), the Hamburg Bright Quasar Survey (Wisotzki et al. 1996) and the Magellan survey (Wisotzki et al. 2004, and references therein). The Jodrell Bank-VLA Astrometric Survey (JVAS;

★ E-mail: aagnello@eso.org
† Hubble Fellow.
‡ Packard Fellow.

[1] The probability of finding a quasar strongly lensed by a cluster is 1–2 orders of magnitude smaller than that by a galaxy, with only a few of the first systems known (e.g. Inada et al. 2003, 2006).

© 2017 The Author(s)
Published by Oxford University Press on behalf of the Royal Astronomical Society

Downloaded from https://academic.oup.com/mnras/article-abstract/474/3/3391/4644836 by Divisione Cood. Biblioteche Uni Statale user on 27 November 2018

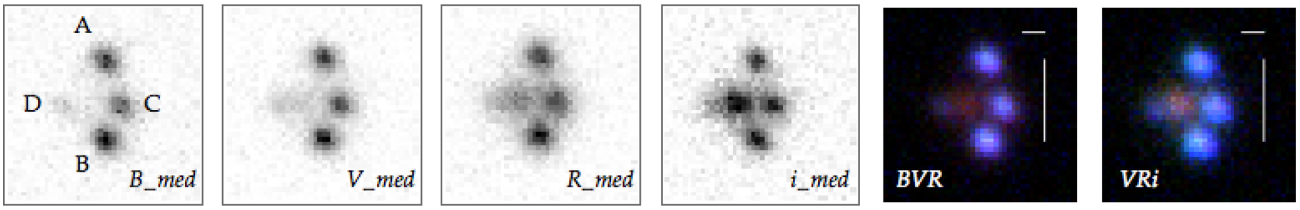

Figure 1. ALFOSC *BVRi* median coadds and 'false colour' RGB composites, North is up and East is to the left. In the RGB colour-composites, the horizontal white segment measures 1 arcsec and the vertical segment spans the 3.6 arcsec maximum image separation. A faint arc, barely visible in *B* band, emanates from the northern-most image. The colour-combination chosen here has red $\propto 0.3R_{k,l}$, green $\propto 0.4V_{k,l}$, blue $\propto 1.6B_{k,l}$ at pixel (k, l) in *BVR*, and red $\propto 0.3i_{k,l}$, green $\propto 0.4R_{k,l}$, blue $\propto 1.6V_{k,l}$ at pixel (k, l) in *VRi*. This colour-code is chosen mostly for visual convenience, to mitigate the effects of sky noise, zero-point and site-specific extinction, making quasars appear 'blue' and early-type galaxies 'red': the quantitative information, consisting in object magnitudes, is given in Table 1.

King et al. 1999) and the Cosmic Lens All-Sky Survey (CLASS; Browne et al. 2003; Myers et al. 2003) targeted flat-spectrum radio-loud sources that could be resolved into multiple components in follow-up observations. The Sloan Quasar Lens Search (SQLS, Oguri et al. 2006) and its successor (BQLS, More et al. 2016) targeted objects with pre-existing quasar fibre-spectra, themselves based on ultraviolet excess (UVx) pre-selection. Optical and radio lens surveys are affected by different systematic effects, and it is thus fundamental to operate with samples of lenses selected from well-characterized populations of sources. The redshift distribution of sources is not the same across different searches, and can peak at lower redshifts than those predicted by OM10: in the SQLS, the source redhift distribution peaks at $z_s \approx 1.95$ (respectively, $z_s \approx 1.5$) for the statistically complete (respectively, full) sample.

Extensions of lens searches to higher completeness must rely solely on photometric pre-selection with limited UVx information. In view of current and upcoming wide-field surveys, diverse techniques have been developed to this aim. Searches tailored on the morphology of quasar lenses rely either on visual inspection of thousands of blue-near-red targets (Lin et al. 2017) or direct modelling of 10^5 image cutouts (Morgan et al. 2004; Schechter et al. 2016). Data-mining techniques have been applied to catalogue magnitudes in the optical and infra-red, by selecting either large samples of quasar-like objects (Ostrovski et al. 2017) or objects resembling simulated lenses (Agnello et al. 2015a; Williams, Agnello & Treu 2017). Lensed quasar selection via variability has been suggested (Kochanek et al. 2006), exploiting difference-imaging in multi-epoch surveys.

Here, we report on the discovery and follow-up of a quadruply lensed quasar, J1433+6007 (shown in Fig. 1), mined with a novel outlier-selection technique in the Sloan Digital Sky Survey (SDSS, Abazajian et al. 2009) DR12 footprint without spectroscopic or UVx information. The two brightest images are separated by ≈3.6 arcsec, the source redshift from the discovery spectra is $z_s = 2.737 \pm 0.003$, and the lens redshift is $z_l = 0.407 \pm 0.002$ from follow-up Keck-ESI spectroscopy. We describe the target/candidate selection procedure in Section 2, the confirmation and follow-up of J1433+6007 in Section 3, and first lens models in Section 4. We conclude in Section 5. In what follows, SDSS magnitudes are in the AB system, WISE (Wright et al. 2010) magnitudes in the Vega system, and where necessary we adopt concordance cosmological parameters $\Omega_\Lambda = 0.7$, $\Omega_m = 0.3$, $H_0 = 70\,\mathrm{km\,s^{-1}\,Mpc^{-1}}$.

2 CANDIDATE SELECTION

Since half of the known quasar lenses in SDSS have extended morphology, due to the presence of the deflector (see Williams et al. 2017, for a discussion), objects with[2] $\log \mathcal{L}_{\mathrm{star},i} < -11$ or `psf_i-mod_i` > 0.075, `mod_i` < 20.5, and WISE colours $W1 - W2 > 0.55$, $W2 - W3 < 3.1 + 1.5(W1 - W2 - 1.075)$ were pre-selected. The i −band selection is used as a morphological pre-selection, whereas the WISE cuts are an extension of those by Assef et al. (2013) to exclude most quasars at $z < 0.35$ and narrow-line galaxies. Quasar lens *targets* were then selected based on their catalogue magnitudes, then visually inspected to exclude obvious contaminants, yielding the final *candidate* sample. Candidates themselves were assigned a grade from 1 (dubious) to 3 (almost surely a lens), based on visual inspection by two investigators.

Lensed quasars are rare among quasars, which, in turn, are rarer than blue galaxies, hence we used a novel outlier selection to mine targets, retaining peculiar objects by excluding more common ones. The improvement in false-positive rejection upon established searches in the SDSS, such as the SQLS, was a requirement for the method to be applicable, in practice, to a wide-field search relying only on photometry, without any UVx or fibre-spectroscopy information. When tested on the SQLS morphologically selected lens candidates of Inada et al. (2012), this procedure recovered 9 of the 10 lenses and excluded half of their 40 false positives.

The method is described elsewhere (Agnello 2017); here we summarize it. Four main classes of 'common' objects were defined, roughly corresponding to nearby ($z < 0.75$) quasars, isolated quasars at higher ($z \approx 2$) redshift, blue-cloud galaxies and faint ($W2 \gtrsim 15$) objects. Each class k was represented by a single Gaussian with mean $\boldsymbol{\mu}_k$ and covariance $\boldsymbol{C}_k$ in a space given by $g - r$, $g - i$, $r - z$, $i - W1$, $W1 - W2$, $W2 - W3$, $W2$ and each object $\boldsymbol{f}$ was assigned pseudo-distances defined as $d_k = 0.5\,\langle \boldsymbol{f} - \boldsymbol{\mu}_k, \boldsymbol{C}_k^{-1}(\boldsymbol{f} - \boldsymbol{\mu}_k)\rangle$. Objects that were 'far' enough from the four class centres, based on linear combinations of their d_k values, were retained as targets.

This yielded ≈250 candidates brighter than $i = 20.0$ over the whole SDSS–DR12 footprint, of which ≈40 known quasar lenses or pairs.[3] J1433+6007, at RA = 14:33:22.8, Dec. = +60:07:13.44 (J2000), showed two well-separated blue images on either sides of two red objects, blended in three photometric components by the SDSS pipeline. It received grades 2 and 3 and was initially

[2] Here $\mathcal{L}_{\mathrm{star},i}$ is the pipeline-estimated probability that an object is a single point-source; details on stellarity and model/psf magnitudes can be found in the SDSS schema browser.

[3] The exact numbers depend on the pseudo-distance cuts chosen in this search, and visual-inspection. In this search, the final sample had 253 candidates and 38 known lenses/pairs.

Downloaded from https://academic.oup.com/mnras/article-abstract/474/3/3391/4644836 by Divisione Cood. Biblioteche Uni Statale user on 27 November 2018

prioritized for follow-up in 2016 June, but observations were weathered out.

3 FOLLOW-UP

Long-slit discovery spectra were obtained on 2017 January 19 and 20 as part of a candidate lens follow-up program (P42−019, PI Grillo), using the Andalucia Faint Object Spectrograph and Camera (ALFOSC) at the 2.5 m Nordic Optical Telescope (NOT) in La Palma (Spain). Standard IRAF routines were used for bias subtraction, flat-field corrections, and wavelength calibration. From ALFOSC *BVRi* imaging, we obtained the positions and magnitudes subsequently used for lens models. Deeper, high-resolution spectroscopy was obtained with the Echellette Spectrograph and Imager (ESI) at the Keck II telescope on 2017 January 20 (PI Jones), and reduced with ESIREDUX.[4]

In what follows, quasar images are labelled A, B, C, D in order of expected arrival time (see Fig. 1). ALFOSC pixels measure 0.21 arcsec per side.

3.1 NOT discovery and follow-up spectra

We used the 1 arcsec-wide long-slit with the #4 grism, covering a wavelength range $3200 < \lambda < 9600$ Å with a dispersion of 3.3 Å pixel^{-1} and resolution $R = 360$. We took two 600 s exposures with the slit aligned north–south, through 14:33:22.8+60:07:13.44, and one (900 s) with east-west alignment, through 14:33:22.8+60:07:14.5. This enabled simultaneous spectroscopy of the two prominent quasar images and the two red objects, respectively. Arc (HeNe, Ar) and flat lamps were used for calibrations. Sky lines around 6000 Å were used to assess the accuracy of wavelength calibration. While flux-calibrated, bandpass-calibrated spectra are useful for studies of variability and continuum spectral shape, lens confirmation requires only that all images correspond to the same source, and hence their spectra have the same redshift, line shape, and flux ratios smoothly varying with wavelength (barring chromatic effects from differential extinction and microlensing). Since bandpass corrections and standard-star calibrations apply the same multiplication to all spectra, and so are not necessary for lens confirmation purposes, we preferred to use the available telescope time to obtain deeper spectroscopic and imaging data once the lens was already confirmed. Following Agnello et al. (2015b), the spectra were modelled as a superposition of multiple Gaussian sources, in order to accurately deblend different traces.

The north–south spectra show three nearly identical traces corresponding to the same $z_s = 2.737 \pm 0.003$ quasar (Fig. 2, top panel), as evaluated on Ly α and C IV. The bright, outer traces correspond to the blue images (A,B) visible in the SDSS. The central, fainter trace is given by a third quasar image C, corresponding to the westmost red object, just outside the slit, thus confirming J1433+6007 as a multiply imaged quasar. The east–west spectra (Fig. 2, middle panel) show clear traces corresponding to images C,D and the lens galaxy (G). Images A,B have almost indistinguishable spectra, with uniform flux ratio ≈1.05, whereas image C undergoes substantial extinction bluewards of C III]. There are ≈5 − 10 per cent flux-ratio differences between the continua and emission lines (Fig. 2, bottom panel), which can be explained as an effect of microlensing.

[4] Available at http://www2.keck.hawaii.edu/inst/esi/ESIRedux/

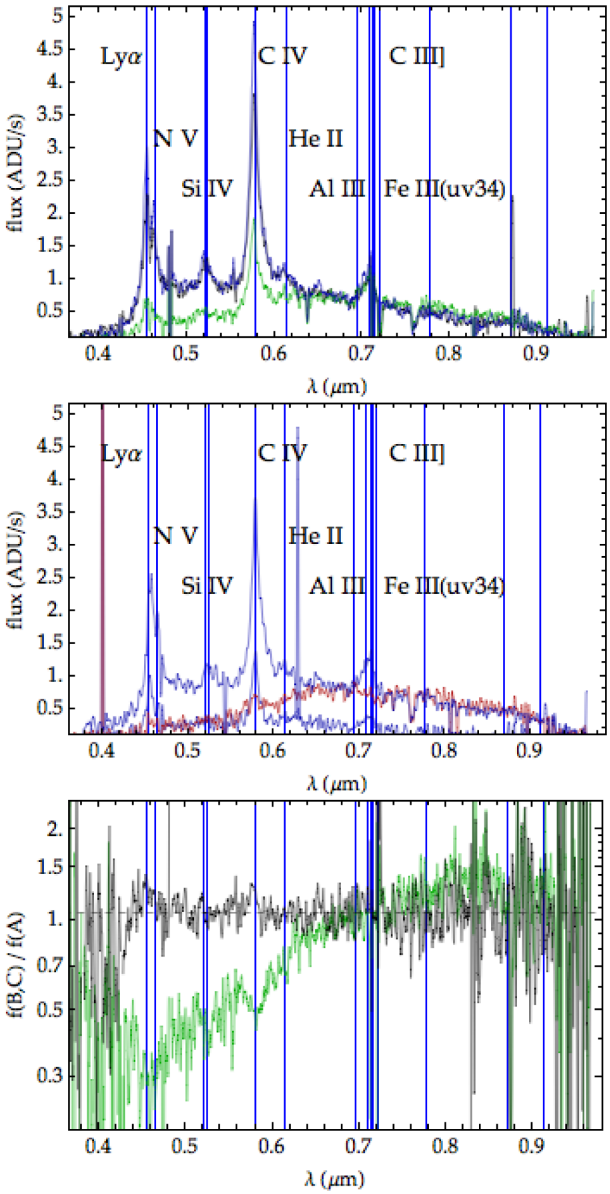

Figure 2. ALFOSC discovery spectra. North–south (top panel) and east–west spectra (*centre*), and flux-ratios of spectra in north–south slit (bottom panel). Image C leaks in the north–south slit and is significantly reddened (green line), whereas images A,B have almost indistinguishable spectra (black line). The source has $z_s = 2.737 \pm 0.003$, as evaluated on Lyα and C IV. The lens galaxy spectrum, with a shape that is well distinguishable from those of the quasar images, is traced in red for the reader's convenience.

3.2 NOT imaging

Follow-up imaging data with good seeing (≈0.6 arcsec full width at half-maximum at Zenith) were obtained with ALFOSC in *B*, *V*, *R*, *i* bands, using multiple 60 s exposures per band. Standard PYTHON routines were used for bias subtraction, flat-fielding and coadding. The median coadds and colour-composites are shown in Fig. 1, where Ly α from the quasar images dominates in *B*band and the lens brightens up in redder bands.

The relative displacements are obtained both from imaging and spectroscopic data. Individual traces in the spectra are well described by Gaussians in the spatial direction, whose run with wavelength can be modelled with uncertainties as low as

Downloaded from https://academic.oup.com/mnras/article-abstract/474/3/3391/4644836 by Divisione Cood. Biblioteche Uni Statale user on 27 November 2018

Table 1. Image positions, *BVRi* magnitudes, and model-predicted values of (point-source) magnifications and time-delays. The nominal errors on some magnitudes would be smaller than quoted, but are limited by the accuracy of the ALFOSC zero-points and observing sky conditions.

Image	δx(arcsec) $= -\cos(\text{Dec.})\delta\text{RA}$	δy(arcsec) $= \delta\text{Dec.}$	B (mag)	V (mag)	R (mag)	i (mag)	μ	$t - t_A$ (d)
A	0.00 ± 0.025	0.00 ± 0.025	20.26 ± 0.04	19.78 ± 0.01	19.26 ± 0.01	19.32 ± 0.01	2.53 ± 0.17	0.00
B	− 0.070 ± 0.025	− 3.650 ± 0.025	20.09 ± 0.03	19.63 ± 0.01	19.13 ± 0.01	19.10 ± 0.01	3.51 ± 0.25	16.0 ± 5.0
C	0.766 ± 0.025	− 2.056 ± 0.025	20.50 ± 0.05	19.92 ± 0.01	19.30 ± 0.01	19.14 ± 0.01	− 2.91 ± 0.60	26.0 ± 5.0
D	− 2.138 ± 0.050	− 2.132 ± 0.050	22.00 ± 0.14	21.30 ± 0.02	20.63 ± 0.02	20.38 ± 0.01	− 0.60 ± 0.10	113.0 ± 5.0
G	− 1.152 ± 0.025	− 1.950 ± 0.025	21.87 ± 0.15	20.69 ± 0.12	19.39 ± 0.01	18.52 ± 0.01	–	–

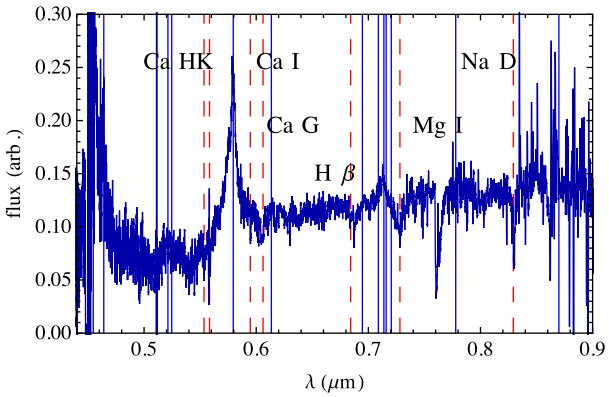

Figure 3. ESI follow-up spectra, with prominent absorption features at $z_l = 0.407 \pm 0.002$, which we associate with G. *Red dashed* lines: Ca HK, *G*-band λ4304, Mg I, Na D absorption at z_l. *Blue solid* lines: quasar emission at z_s. The Ca HK complex is visible, albeit at lower signal-to-noise ratio, also in the ALFOSC spectra.

0.125 pixels = 25 mas. Uncertainties from imaging-only data, though nominally smaller, are dominated by systematics from different noise realizations. Residuals between imaging data and model, mostly due to faint features and PSF mismatch, are within the noise level.

Table 1 gives the positions of the four images (A,B,C,D) and deflector (G), relative to image A, and *BVRi* magnitudes. Images C and D are substantially reddened, and blending between D and G is significant in *B* band.

3.3 Keck-ESI follow-up

ESI spectra of G were taken in echellette mode, with 1.0 arcsec slit-width oriented east–west and resolution $R = 4900$, roughly constant to within 10 per cent over the whole spectral range. The total integration time was 45 min split into three exposures of 900 seconds each. Bias and dark subtraction, flat-field correction, sky subtraction, and spectral extraction are performed directly by ESIREDUX. The combined 1D spectrum of G and D, shown in Fig. 3, has distinctive absorption features at $z_l = 0.407 \pm 0.002$ (Ca HK, *G* band, H β, Mg I/Fe complex, Na D), which we associate with the lens galaxy. The same features could be seen in the ALFOSC discovery spectra, although not as clearly.

We measured the lens velocity dispersion by fitting a Gaussian profile to the Ca K line, yielding $\sigma_{\rm los} = (216 \pm 55)\,{\rm km\,s^{-1}}$. This corresponds to the integrated velocity dispersion within a 1 arcsec wide spectroscopic aperture centred on the lens galaxy G, which is partly blended with image D due to ∼1 arcsec seeing.

Table 2. Lens model parameters: best fit (first column) and 68 per cent confidence intervals, marginalized over other parameters. Tight (and expected) degeneracies among parameters are present, given in equation (2), except for the combination $\theta_{\rm E}$, which corresponds to the Einstein radius. Angles ϕ_l, ϕ_s are positive counter-clockwise from West.

	$\theta_{\rm E}$	q	ϕ_l	ϕ_s	γ_s
best	1.80 arcsec	0.50	0.18[rad]	1.12[rad]	0.10
68 per cent low	1.70 arcsec	0.43	0.13[rad]	0.96[rad]	0.08
68 per cent high	1.90 arcsec	0.58	0.25[rad]	1.22[rad]	0.13

4 LENS MODELS

From the relative displacements in Table 1, we fit a simple lens model to obtain the enclosed (2D) mass and predicted magnifications and time-delays. We do a conjugate-point analysis using GLEE (Suyu & Halkola 2010; Suyu et al. 2012), adopting 25 mas uncertainties on the positions of A,B,C and G, and 50 mas uncertainties on the position of image D. We do not fit to the flux-ratios, as, in general, they can be significantly affected by differential extinction, microlensing, and time-delays, and we can expect this to happen also in this case from the ratio of spectra shown in Fig. 2.

The surface density of the lens is described by

$$\kappa(x, y) = \frac{\Sigma(x, y)}{\Sigma_{\rm cr}} = \frac{b}{2\sqrt{X^2/(1+e)^2 + Y^2/(1-e)^2}} \qquad (1)$$

(Kassiola & Kovner 1993), along the principal axes of G, where $\Sigma_{\rm cr} = c^2 D_s/(4\pi G\, D_l D_{ls})$ factors the dependence on angular-diameter distances. The coordinates (X, Y) are rotated from the standard coordinates ($\delta x = -\cos(\text{Dec.})\delta\text{RA}$, $\delta y = \delta\text{Dec.}$) by an angle ϕ_l. The Einstein radius is defined as the geometric mean of the major and minor axes of the critical curve, $\theta_{\rm E} = 2b\sqrt{q}/(1+q)$. We include external shear, with amplitude γ_s and angle ϕ_s, and allow all parameters to vary freely, including the lens flattening $q = (1-e)/(1+e)$ and position angle ϕ_l. The models then have seven parameters (b, ϕ_l, q, ϕ_s, γ_s, and the source position) and eight constraints with uncertainties (the relative displacements of the four image positions). The lens centre, nominally adding two free parameters, is already well constrained within (at most) 0.05 arcsec by the ALFOSC cutout models (Table 1).

The results are summarized in Tables 1and 2, and Fig. 4. The Einstein radius is robustly determined to $\theta_{\rm E} = (1.80 \pm 0.10)$ arcsec, very close to half the A–B separation and independent of other inferred quantities. Flux-ratios from the best-fitting model are comparable to those measured in *i* band, accounting for differential extinction whose existence in lensing is well established (e.g. Falco et al. 1999; Mediavilla et al. 2005; Elíasdóttir et al. 2006; Agnello et al. 2017). The predicted delays $t_D - t_A > 100$ d, $t_C - t_A \approx 25$ d can be accurately measured in one or two seasons of high-cadence monitoring.

Downloaded from https://academic.oup.com/mnras/article-abstract/474/3/3391/4644836 by Divisione Cood. Biblioteche Uni Statale user on 27 November 2018

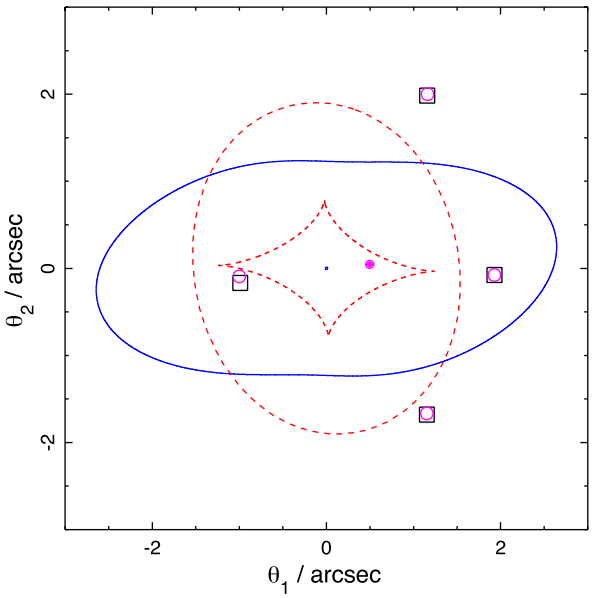

Figure 4. Lens model results: observed image positions (open squares), model-predicted images (open circles) and lens centre (blue point), inferred source position (fuchsia bullet), critical curve (blue), and radial and astroid caustics (red). The position of image D is slightly biased, due to blending with G, but is recovered within the adopted uncertainties. The axes mark $\theta_1 = -\cos(\text{Dec.})\delta\text{RA}$ and $\theta_2 = \delta\text{Dec}$.

Monopole–quadrupole degeneracies (e.g. Kochanek 2006) are present, in particular,

$$\gamma_s \approx 0.10 + 0.35(q - 0.5),$$
$$\phi_s \approx 1.1 - 1.5(b - 2.5),$$
$$\gamma_s \approx 0.10 + 0.35(\phi_l - 0.18), \quad (2)$$

for this system. These may be broken with: observations of the line-of-sight environment, to characterize external contributions to the deflections; and higher resolution imaging, of both the lensed quasar host and of G, to disentangle shear and lens flattening. Significant quadrupole, in the form of external shear or ellipticity, is not unexpected in quasar lenses (Keeton, Kochanek & Seljak 1997; Holder & Schechter 2003), and, in fact, multipole contributions can, in general, be enough to appreciably affect flux ratios (Xu et al. 2015; Hsueh et al. 2016; Gilman et al. 2017)

The velocity dispersion σ of stars in the lens is a useful observable that can be estimated from the lens model itself. A direct measurement of σ and its comparison with predictions from lensing can be used to measure cosmological distances and to constrain the dark matter density profile of the lens (Treu & Koopmans 2004; Grillo, Lombardi & Bertin 2008; Paraficz & Hjorth 2009; Suyu et al. 2014; Sonnenfeld et al. 2015; Jee et al. 2016). In the singular isothermal sphere (SIS) limit $q \to 1$, σ depends weakly on location[5] and is well approximated by

$$\sigma_{\rm sis}^2 = \frac{c^2 \theta_{\rm E} D_{\rm s}}{4\pi D_{\rm ls}} \,. \quad (3)$$

With the above values, we then obtain $\sigma = (290 \pm 8)\,\mathrm{km\,s^{-1}}$, as expected for massive ellipticals (Treu et al. 2005). A direct comparison between the estimate in equation (3) and direct measurements will need dynamical models that encompass asphericity and inclination effects (Barnabè et al. 2011), as well as a more accurate measurement of σ from deeper spectra with a robust subtraction of the quasar contamination.

[5] The details depend on the steepness of the starlight's profile and the orbital anisotropy (Barnabè et al. 2011).

5 DISCUSSION AND CONCLUSIONS

Lensed quasars are rare, and quadruply lensed quasars are even rarer. Assembling homogeneous sets of quasar lenses, with a selection function that can be well characterized and with the capability of discovering 'new' quads, is paramount to different lines of investigation (microlensing, substructure lensing, cosmography) that require samples of ≈40 lenses each, with suitable ancillary data. The advent of wide-field surveys helps overcome the rarity of these systems, provided lens searches can be performed on photometric data and recover systems to a good completeness level, spanning source redshifts $z_s > 2$, where most lenses are expected to lie.

We have found a new, quadruply lensed quasar at RA = 14:33:22.8, Dec. = +60:07:14.5, via an outlier-selection procedure applied to the SDSS–DR12 photometric footprint (detailed by Agnello 2017). Similar to other recent, wide-field photometric searches, this search did not rely on previous spectroscopic or UV excess information. This approach enables the discovery of systems with sources at higher redshifts than typically probed, and with appreciable differential reddening by the lens galaxy. This aspect is particularly relevant if, for example, microlensing or substructure studies are concerned, since one needs to ensure that the samples themselves are not biased against systems with significant departures from the simplest image and flux-ratio configurations.

Discovery NOT–ALFOSC data confirmed this system as a lens with $z_s = 2.737$ and four images on a fold configuration. The lens redshift is $z_l = 0.407$ from follow-up Keck-ESI spectroscopy, which together with the lens model results with $\theta_{\rm E} = (1.80 \pm 0.10)$ arcsec predicts a velocity dispersion $\sigma = (290 \pm 9)\,\mathrm{km\,s^{-1}}$. The velocity dispersion measured from ESI data, within a 1 arcsec aperture in 1 arcsec seeing conditions, is $\sigma_{\rm los} = (216 \pm 55)\,\mathrm{km\,s^{-1}}$, but deeper data in better seeing are needed, to accurately correct for contamination by the quasar images (C,D) and model aperture effects. Saddle-point images C,D are significantly reddened by the lens galaxy, while the A/B flux ratios agree with predictions by the lens model within ≈0.1 mag.

This lens is then relevant to multiple applications. Microlensing is evident in the differential magnification of lines and continua, and it can yield a determination of the stellar mass fraction in a galaxy at $z_s \approx 0.4$ if deeper spectroscopic data are obtained. The expected time-delays (Table 1) can be measured accurately with high-cadence campaigns spanning one or two monitoring seasons, making this system an ideal lens for a cosmographic sample. With current data, significant monopole-quadrupole degeneracies arise in the lens model, but they can be broken with deeper and higher resolution follow-up. This, in turn, will reduce the systematic errors in the lens macro-model, with applications to the study of dark matter density profiles, time-delay cosmography, microlensing, and detection of substructure.

ACKNOWLEDGEMENTS

CG and MB acknowledge support by VILLUM FONDEN Young Investigator Programme through grant no. 10123. TJ acknowledges support provided by NASA through Program # *HST*-HF2-51359 through a grant from the Space Telescope Science Institute, which is

Downloaded from https://academic.oup.com/mnras/article-abstract/474/3/3391/4644836 by Divisione Cood. Biblioteche Uni Statale user on 27 November 2018

operated by the Association of Universities for Research in Astronomy, Inc., under NASA contract NAS 5-26555. TT acknowledges support by the Packard Foundation through a Packard Research Fellowship and by the National Science Foundation through grant AST-1450141. SHS gratefully acknowledges support from the Max Planck Society through the Max Planck Research Group.

The data presented here were obtained in part with ALFOSC, which is provided by the Instituto de Astrofisica de Andalucia (IAA) under a joint agreement with the University of Copenhagen and NOTSA. We thank R.T. Rasmussen and T. Pursimo for support at the NOT.

Some of the data presented herein were obtained at the W. M. Keck Observatory, which is operated as a scientific partnership among the California Institute of Technology, the University of California and the National Aeronautics, and Space Administration. The Observatory was made possible by the generous financial support of the W. M. Keck Foundation. The authors wish to recognize and acknowledge the very significant cultural role and reverence that the summit of Maunakea has always had within the indigenous Hawaiian community. We are most fortunate to have the opportunity to conduct observations from this mountain.

REFERENCES

Abazajian K. N. et al., 2009, ApJS, 182, 543
Agnello A., Kelly B. C., Treu T., Marshall P. J., 2015, MNRAS, 448, 1446
Agnello A. et al., 2015, MNRAS, 454, 1260
Agnello A., Sonnenfeld A., Suyu S. H., Treu T., Fassnacht C. D., Mason C., Bradač M., Auger M. W., 2016, MNRAS, 458, 3830
Agnello A. et al., 2017, MNRAS, 472, 4038
Agnello A., 2017, MNRAS, 471, 2013
Assef R. J. et al., 2013, ApJ, 772, 26
Barnabè M., Czoske O., Koopmans L. V. E., Treu T., Bolton A. S., 2011, MNRAS, 415, 2215
Braibant L., Hutsemékers D., Sluse D., Anguita T., 2016, A&A, 592, A23
Browne I. W. A. et al., 2003, MNRAS, 341, 13
Chan J. H. H. et al., 2015, ApJ, 807, 138
Courbin F., Saha P., Schechter P. L., 2002, Gravitational Lensing: Astrophys Tool, 608, 1
Dalal N., Kochanek C. S., 2002, ApJ, 572, 25
Elíasdóttir, Á., Hjorth J., Toft S., Burud I., Paraficz D., 2006, ApJS, 166, 443
Falco E. E. et al., 1999, ApJ, 523, 617
Gilman D., Agnello A., Treu T., Keeton C. R., Nierenberg A. M., 2017, MNRAS, 467, 3970
Grillo C., Lombardi M., Bertin G., 2008, A&A, 477, 397
Holder G. P., Schechter P. L., 2003, ApJ, 589, 688
Hsueh J.-W., Fassnacht C. D., Vegetti S., McKean J. P., Spingola C., Auger M. W., Koopmans L. V. E., Lagattuta D. J., 2016, MNRAS, 463, L51
Inada N. et al., 2003, AJ, 126, 666
Inada N. et al., 2006, ApJL, 653, 97
Inada N., Oguri M., Shin M.-S. et al., 2012, AJ, 143, 119
Jee I., Komatsu E., Suyu S. H., Huterer D., 2016, J. Cosmol. Astropart. Phys., 4, 031
Kassiola A., Kovner I., 1993, Liege Int. Astrophys. Colloquia, 31, 571
Keeton C. R., Kochanek C. S., Seljak U., 1997, ApJ, 482, 604
King L. J., Browne I. W. A., Marlow D. R., Patnaik A. R., Wilkinson P. N., 1999, MNRAS, 307, 225
Kochanek C. S., 2003, ApJ, 583, 49
Kochanek C. S., 2004, ApJ, 605, 58
Kochanek C. S., 2006, Saas-Fee Advanced Course 33: Gravitational Lensing: Strong, Weak and Micro, 91
Kochanek C. S., Mochejska B., Morgan N. D., Stanek K. Z., 2006, ApJ, 637, L73
Lin H. et al., 2017, ApJ, 838, L15
Mao S., Schneider P., 1998, MNRAS, 295, 587
Maoz D., Bahcall J. N., Doxsey R., Schneider D. P., Bahcall N. A., Lahav O., Yanny B., 1992, ApJ, 394, 51
Mediavilla E., Muñoz J. A., Kochanek C. S., Falco E. E., Arribas S., Motta V., 2005, ApJ, 619, 749
Ménard B., Scranton R., Fukugita M., Richards G., 2010, MNRAS, 405, 1025
More A., McKean J. P., More S., Porcas R. W., Koopmans L. V. E., Garrett M. A., 2009, MNRAS, 394, 174
More A. et al., 2016, MNRAS, 465, 2411
Morgan N. D., Caldwell J. A. R., Schechter P. L., Dressler A., Egami E., Rix H.-W., 2004, AJ, 127, 2617
Myers S. T. et al., 2003, MNRAS, 341, 1
Nierenberg A. M., Treu T., Wright S. A., Fassnacht C. D., Auger M. W., 2014, MNRAS, 442, 2434
Oguri M., Marshall P. J., 2010, MNRAS, 405, 2579 (OM10)
Oguri M. et al., 2006, AJ, 132, 999
Ostrovski F. et al., 2017, MNRAS, 465, 4325
Paraficz D., Hjorth J., 2009, A&A, 507, L49
Refsdal S., 1964, MNRAS, 128, 307
Rusu C. E., Oguri M., Minowa Y., Iye M., More A., Inada N., Oya S., 2014, MNRAS, 444, 2561
Schechter P. L., Morgan N. D., Chehade B., Metcalfe N., Shanks T., McDonald M., 2016, AJ, 153, 219
Sonnenfeld A., Treu T., Marshall P. J., Suyu S. H., Gavazzi R., Auger M. W., Nipoti C., 2015, ApJ, 800, 94
Suyu S. H., Halkola A., 2010, A&A, 524, A94
Suyu S. H. et al., 2012, ApJ, 750, 10
Suyu S. H. et al., 2014, ApJ, 788, L35
Treu T., Koopmans L. V. E., 2004, ApJ, 611, 739
Treu T. et al., 2005, ApJ, 633, 174
Walsh D., Carswell R. F., Weymann R. J., 1979, Nature, 279, 381
Wambsganss J., 2001, PASA, 18, 207
Williams P., Agnello A., Treu T., 2017, MNRAS, 466, 3088
Wisotzki L., Koehler T., Groote D., Reimers D., 1996, A&AS, 115, 227
Wisotzki L., Schechter P. L., Chen H.-W., Richstone D., Jahnke K., Sánchez S. F., Reimers D., 2004, A&A, 419, L31
Wright E. L. et al., 2010, AJ, 140, 1868
Xu D., Sluse D., Gao L., Wang J., Frenk C., Mao S., Schneider P., Springel V., 2015, MNRAS, 447, 3189

This paper has been typeset from a TEX/LATEX file prepared by the author.

Downloaded from https://academic.oup.com/mnras/article-abstract/474/3/3391/4644836 by Divisione Cood. Biblioteche Uni Statale user on 27 November 2018